La Metallurgia Italiana
International Journal of the Italian Association for Metallurgy

Effect of macro- and microstructural features on the corrosion behavior of additively manufactured alloy 625

F. Carugo, M. Cabrini, A. Carrozza, S. Lorenzi, T. Pastore, G. Barbieri, F. Cognini, M. Moncada

The aim of the work is to investigate the general and localized corrosion behavior of Alloy 625 obtained via different AM technologies, namely laser powder bed fusion (LPBF) and metal fused filament fabrication (MFFF). The outcomes of these evaluations were compared with the traditionally manufactured material (hot rolling). The macro- and microstructures as well as unique surface features of the AM-produced spec-imens were assessed in terms of digital optical microscopy and scanning electron microscopy. Intergranu-lar corrosion susceptibility tests, in compliance with ASTM G28 method A (1), potentiodynamic and poten-tiostatic polarization tests were performed. The electrochemical tests were carried out in sulfuric acid ac-cording to the ASTM G5 standard (2) and in deaerated chloride solutions. The results demonstrated that the surface features, porosity, as well as the microstructure are strictly dependent upon the manufacturing technology. Corrosion morphologies change significantly in function of the unique macro- and microstruc-tural features. Susceptibility to intergranular corrosion tests carried out on the MFFF alloy only revealed not penetrating attack. The results of potentiostatic and potentiodynamic tests showed a passive behavior over a wide range of potentials, thus confirming the very high corrosion resistance to localized corrosion of the additive manufacturing Alloy 625 in neutral chloride solutions. In acidified chloride solution (pH = 3) the presence of crevice attacks on MFFF specimens was detected.

KEYWORDS: ALLOY 625, LASER POWDER BED FUSION, METAL FUSED FILAMENT FABRICATION, CORROSION BEHAVIOR, MACRO- AND MICROSTRUCTURAL FEATURES;

INTRODUCTION

Additive manufacturing (AM) technologies are redefining traditional design and manufacturing strategies, thus granting the possibility to obtain materials and products with high-added value and outstanding performances. These techniques rely on a layer-by-layer approach to generate unique microstructures. Significant efforts have been mainly made by researchers and industry to optimize process parameters and post-processing heat treatments to achieve high mechanical performances. However, also corrosion resistance is fundamental for the alloys adopted in severe operating environments. For these applications, nickel-based Alloy 625 is commonly used owing to its good tensile strength and resistance against chloride-ion stress corrosion cracking and localized corrosion in marine, Oil & Gas industry, and chemical processing environments (3–6).

Marina Cabrini, Francesco Carugo, Alessandro Carrozza, Sergio Lorenzi, Tommaso Pastore
Università di Bergamo

Giuseppe Barbieri, Francesco Cognini, Massimo Moncada
ENEA

Among the AM techniques available, the most widespread are the powder bed-based processes, such as Laser Powder Bed Fusion (LPBF) (7). However, recent techniques combining printing with debinding and sin-tering processes are gaining popularity. Metal Fused Filament Fabrication (MFFF) is an emerging multi-step additive manufacturing process that uses a metal–polymer filament as a feedstock. The paper is devoted to the study of the influence on the corrosion behavior of Alloy 625 of LPBF and MFFF AM-technologies. The outcomes of these evaluations were compared with data published in previous paper (8,9).

MATERIALS AND METHODS

The MFFF-manufactured specimens were built by using a commercial metal powder-polymer filament Mark-forged Inconel 625 that meet chemical requirements of ASTM B443 standard(10), after printing, washing, and sintering (11). An EOS gas atomized powder was used for LPBF specimens. The distribution of the powders size is within the range with a d_{10} of 16 μm and d_{90} of 48 μm. For comparison purpose, a 16 mm diameter hot worked (HW) bar was considered. The bar was supplied in the annealed condition, after a heat treatment at 980 °C for 32 min, followed by water quenching (Grade 1, according to ASTM B446 (12)). The chemical com-positions are reported in Tab. 1.

Tab.1 - Chemical compositions.

Chemical composition of Alloy 625 LPBF powder, composition limits according to ASTM B443 (10) and annealed bar (%wt.)			
Element	**LPBF powder**	**ASTM B443 (10)**	**HW**
C	0.013	0.1 max	0.036
Si	0.1	0.5 max	0.25
Mn	0.03	0.5 max	0.19
P	<0.001	0.015 max	0.007
S	0.002	0.015 max	0.001
Cr	22.8	20.0 – 23.0	21.6
Mo	8.1	8.0 – 10.0	8.26
Ni	64.37 (Balanced)	bal	61.9
Nb	3.66	3.15 – 4.15	3.66
Ti	0.17	0.4 max	0.24
Al	<0.01	0.4 max	0.2
Co	0.17	1.0 max	0.02
Ta	0.13	-	0.01
Fe	0.43	5.0 max	3.1
Nb+Ta	3.79	-	3.67

Specimens

The LPBF specimens were manufactured by using an EOSINT M270 Dual Mode machine, operating in an argon atmosphere. The process parameters and scanning strategy were optimized in order to produce parts with very low porosity, as reported in a previously published work (13). MFFF specimens were obtained by using the Metal X System (Markforged). The manufacturing operation consisted of three main steps: printing a green part of metal powder bound in a polymer matrix, debinding and then sintering to obtain a dense part. The single layer deposition strategy involved the deposition of 4 contouring layers (wall layers) and the filling of the internal section (infill).

Two types of specimens were adopted. Cubic specimens were used for microstructural analysis and immersion test – 15 mm and 16 mm side for LPBF and MFFF processes respectively. Disks height 5 mm were employed for potentiodynamic and potentiostatic polarization tests with 15 mm and 16 mm diameter (for LPBF and MFFF, respectively). 5 mm-tall cylindrical specimens were obtained by cutting the hot-worked bar.

Corrosion tests

Susceptibility to intergranular corrosion tests were performed on the cubic specimens. Boiling ferric sul-fate/sulfuric acid test were carried out according to ASTM G28 standard, method A (1). Before testing, the surfaces of specimens were ground by silicon carbides emery paper up to 1200 grit. Two faces were ground and polished up to 1 μm, using a diamond paste, to allow the observation of corrosion attack mor-phologies on the main planes (parallel and perpendicular to the building direction). Afterwards, the speci-mens were rinsed in water, degreased in an acetone ultrasonic bath and dried before the immersion in the boiling test solution. Before and after tests, the samples were weighed by means of analytic scale to measure the weight loss and corrosion rate. Finally, the specimen was observed using a scanning electron microscope (SEM) in order to investigate the corrosion morphology.

Potentiodynamic and potentiostatic tests were performed on disk specimens. The testing surfaces were firstly ground using SiC emery papers and subsequently polished up to 1 μm diamond paste. Before the tests, all the specimens were ultrasonically cleaned in acetone at room temperature, dried and allowed to passivate in air at room temperature for 1 hour. The tests were performed in a 1-liter standard three elec-trode cell (ASTM G5 (2)) using a PTFE sample holder with a circular exposed area of 10 mm diameter, a Saturated Calomel Electrode (SCE) and two graphite counter electrodes. The testing solution was de-oxygenated by means of nitrogen gas purging, maintained throughout the whole test. A thermostatic water bath provided constant temperatures. The potentiodynamic tests were conducted in three testing solutions:

- 1 N H_2SO_4 solution – according to ASTM G5 (2) at 30°C
- 0.6 M NaCl + HCl, pH 3 at 40°C
- 0.6 M NaCl, pH 7 at 40°C

Before the cyclic potentiodynamic tests, the open circuit potential (OCP) was monitored until stability was achieved. The tests were carried out according to ASTM G5 (2) using a 10 mV/min scan rate. The polariza-tion tests in chloride solution were conducted from 10 mV below the OCP up to 1 V vs. SCE or until the an-odic current density reached 10 mA/cm^2. Afterwards, a reverse scan returned the potential to the initial OCP value.

Potentiostatic tests were carried out in NaCl at pH 7 at +200 mV or +500 mV vs. SCE and in acidified chlo-ride solution at +200 mV vs. SCE for 24 hours, with an acquisition rate of 1 Hz. Before the test, the OCP was monitored for 1 hour.

RESULTS AND DISCUSSION

Fig. 1 shows the micrographs of the MFFF-manufactured specimens realized on the two main planes, i.e., perpendicular (Fig. 1a) and parallel (Fig. 1b) to the building direction. In both cases, there is a continuous pattern of defects due to an incomplete densification of the green part during the sintering process. Particu-larly larger porosities are observed in the external part, in correspondence with the wall layers. This leads to very different porosity values between the external zone (wall layers) and the internal one (infill layers) as shown in Fig. 1c. Through digital image analysis, a porosity value of about 7.7% in the external region was obtained, while in the internal part this value was about 1.1%.

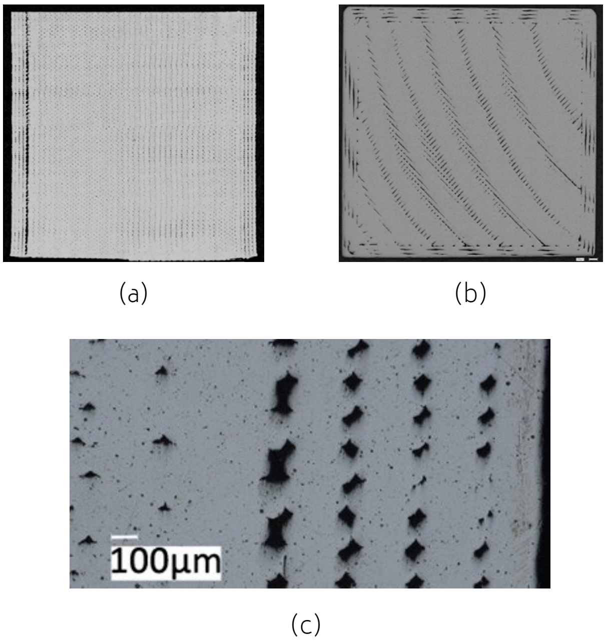

(a) (b)

(c)

Fig.1 - Micrograph of MFFF-manufactured samples: a) perpendicular direction b) parallel direction c) particular of the parallel direction in correspondence with the wall layers

Fig. 2 shows the microstructure obtained after chemical etching. The microstructure of MFFF-processed specimens comprises equiaxed austenite grains, coarser than in the HW condition. This is also completely different from the microstructure observed on the LPBF-manufactured specimens (9), confirming that the microstructure is strictly dependent upon the manufacturing technique adopted.

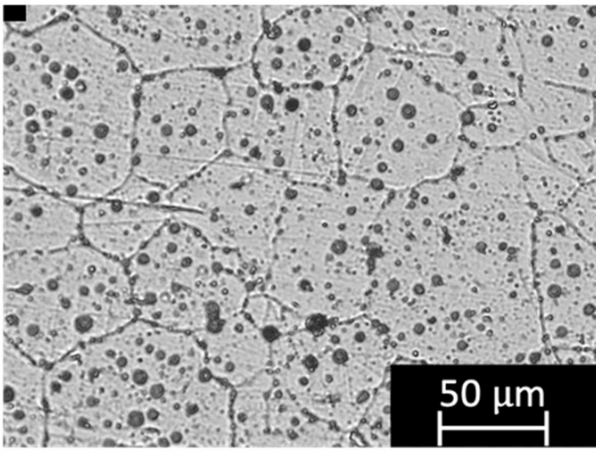

Fig.2 - Representative micrograph of a MFFF-manufactured sample.

Fig. 3 shows the results of the susceptibility to intergranular corrosion test carried out on a MFFF-built specimen in terms of corrosion rate. The results obtained on LPBF and HW specimens and already published in previous work were considered as a comparison (9).

The corrosion rate of the specimens obtained by means MFFF is higher than those obtained for LPBF, but it is still lower than that one obtained on HW specimens.

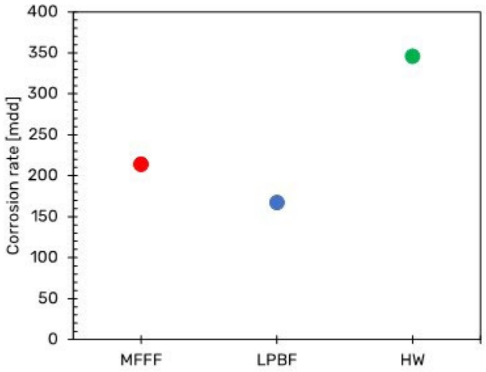

Fig.3 - Results of susceptibility to intergranular corrosion test in boiling sulphate/sulfuric acid solution (ASTM G28, method A (1)).

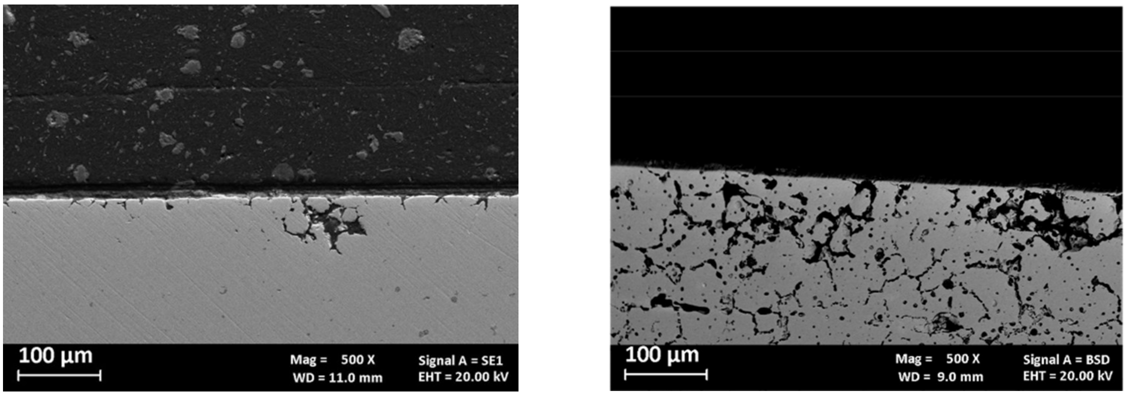

(a) (b)

Fig.4 - SEM images of produced alloy 625 after intergranular corrosion tests. a) metallographic section of the surface along the building direction, b) metallographic section of the surface perpendicular to the building direction.

Fig. 4 show the SEM images of the corrosion morphology of the MFFF-processed specimen after the test. A different morphology was observed on the two main development planes. Only isolated attacks were observed on the surface parallel to the building direction (Fig. 4b). Conversely Fig. 4b showed a higher number of attacks on the surface perpendicular to the building direction, thus confirming that the corrosion behavior is strictly dependent upon the process parameters of the AM technologies adopted.

Some examples of potentiodynamic polarization curves are shown in Fig. 5. Fig. 5a shows the results of the potentiodynamic polarization tests in 1 N H_2SO_4 solution (ASTM G5 (2)) for the specimens obtained by means of MFFF and LPBF and for comparison that of the HW. All the curves show a passive behavior over a wide range of potentials up to an increase in the anodic current density for potential values corresponding to the development of oxygen. This behavior indicates that in this environment the alloy does not undergo corrosion, thus confirming the results obtained in a previous work (8).

Similar results were observed for the MFFF- and LPBF-manufactured specimens in neutral chloride solu-tion in Fig. 5b. The free corrosion potentials were lower than those obtained in the 1N H_2SO_4 solution. The anodic polarization curves showed a wide range of passivity that ended at potential values equal to about +0.5 V vs SCE. This value is lower than the oxygen development potential, indicating the dissolution of the alloy under transpassive conditions. However, by reversing the scanning, the absence of a hysteresis loop and a repassivation potential significantly higher than the initial free corrosion potential is observed. Even in this case, no difference between the specimens obtained by means MFFF and LPBF was observed.

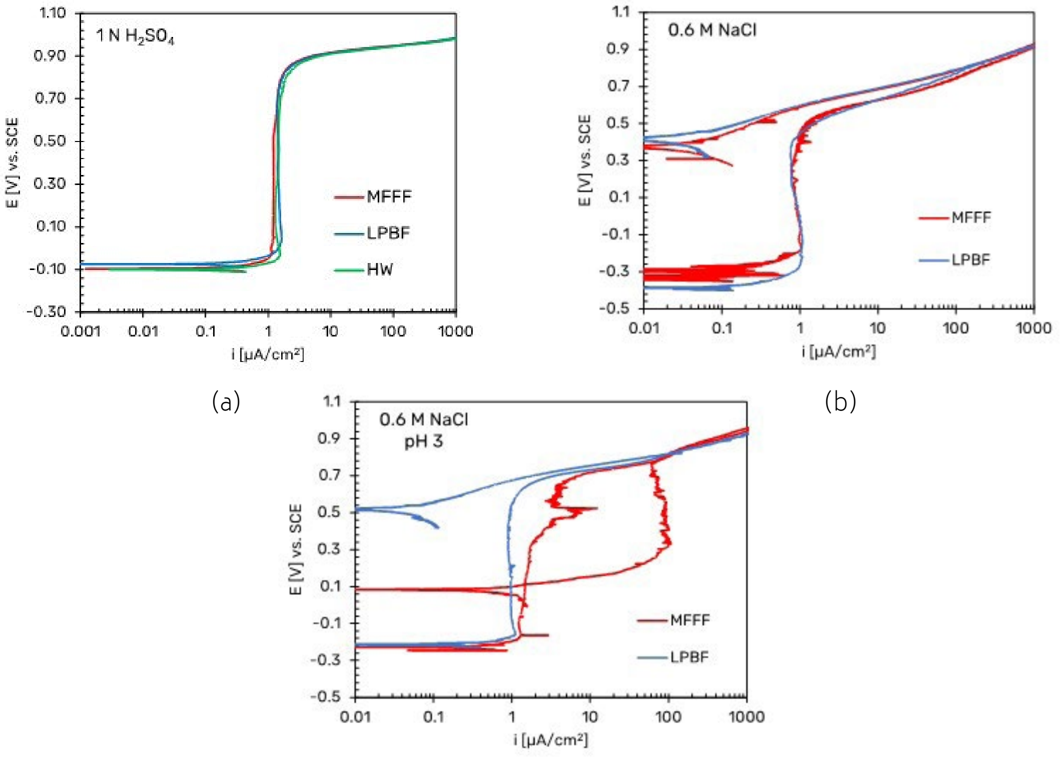

(a) (b)

(c)

Fig.5 - Potentiodynamic polarization curves of Alloy 625 specimens. a) in H_2SO_4 1N, according to ASTM G5 standard (2), b) in neutral 0.6 M NaCl, c) in acidified 0.6 M NaCl at pH 3.

Potentiodynamic tests carried out in 0.6 M NaCl solution at pH 3 showed a free corrosion potential higher than that observed in neutral chloride solution. In this case, a difference between the LPBF and MFFF specimens was observed. The LPBF-manufactured specimen maintain a passive behavior up to the potential of about 0.6 V vs. SCE, after which the anodic current density increases to reach the transpassivity value. The reverse scan curve shows a repassivation without hysteresis and a repassivation potential equal to about 0.5 V vs SCE slightly higher than that one observed in solution at pH 7. Conversely, the specimens obtained by means MFFF show a trend like LPBF only up to potential slightly higher than the free corrosion potential, beyond which a gradual increase in the anodic current density is observed. This deviation increases as the applied potential increases, until the transpassivity potential is sharply reached. The reverse scan curve shows a large hysteresis and repassivation at a lower potential than that one observed on LPBF specimens. This behavior is due to the initiation of crevice corrosion under the gasket in correspondence with a defect present on the surface of the sample as shown in Fig. 6.

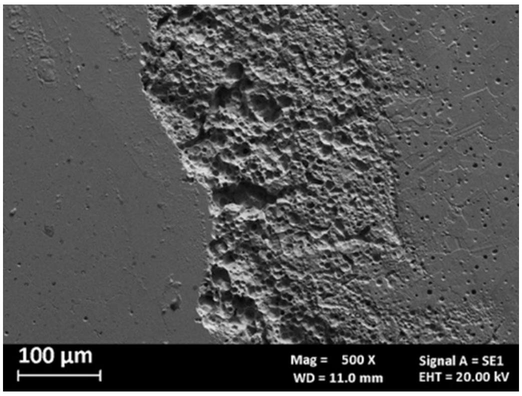

Fig.6 - SEM image of crevice attack on MFFF specimens in acidified chloride solution.

Fig. 7 shows some examples of potentiostatic polarization curves obtained at +200 mV vs SCE in neutral and acidified chloride solutions and at +500 mV vs SCE in neutral 0.6 M NaCl solution.

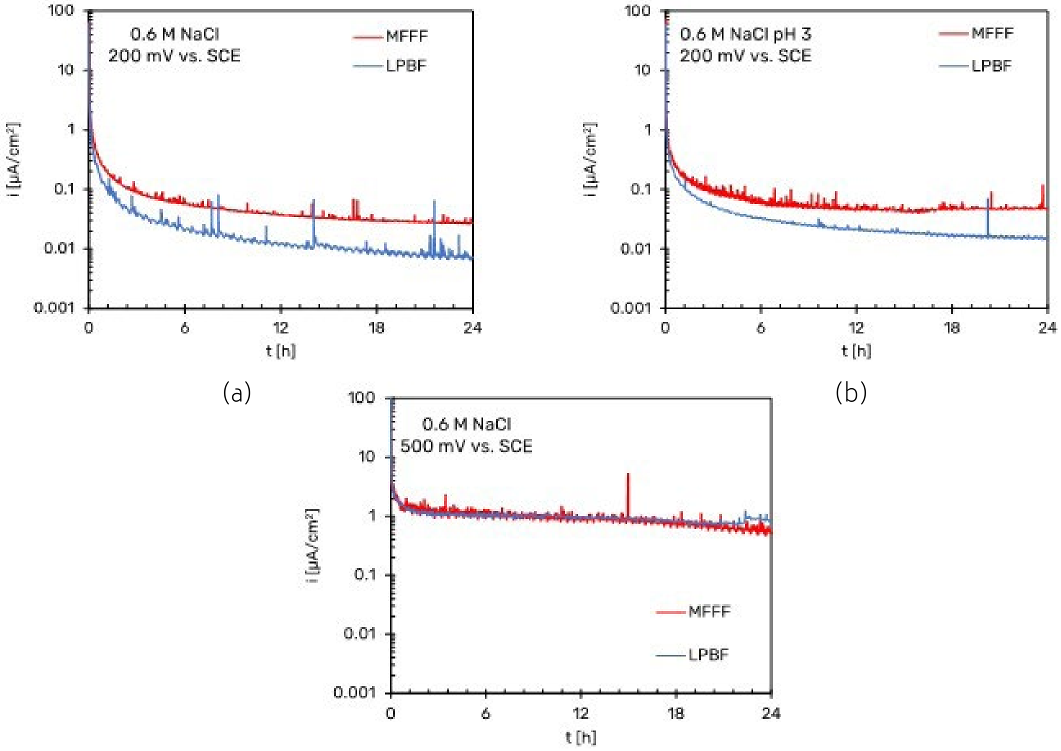

(a) (b)

(c)

Fig.7 - Potentiostatic polarization curves of Alloy 625 specimens. a) +200 mV vs SCE in neutral 0.6 M NaCl, b) +200 mV vs SCE in acidified 0.6 M NaCl at pH 3, c) +500 mV vs SCE in neutral 0.6 M NaCl.

Fig. 7a and b show that the passivity current density for both the MFFF and LPBF specimens is an order of magnitude lower than the current density in the passivity section obtained in the potentiodynamic tests. This is due to the fact that potentiodynamic tests do not allow to evaluate the passive current since they are non-stationary methods. In general, it is observed that the passivity current density value is lower for the LPBF-manufactured specimens than for the MFFF-processed ones, demonstrating a greater corrosion resistance under these conditions. In the tests carried out at +500 mV vs SCE in neutral chloride solution no differences were found between the two AM techniques (Fig. 7c). At this potential value, the passivity current density is an order of magnitude greater than that obtained at +200 mV vs SCE.

In none of the tests carried out a rapid increase in current was observed, thus indicating the absence of a trigger of localized corrosion (pitting or crevice). The presence of many spikes of current density was ob-served, corresponding to the propagation and rapid repassivation of metastable pits (14).

Further potentiostatic tests are planned to investigate the corrosion behavior of alloy 625 produced by addi-tive technologies even at +500 mV vs. SCE.

CONCLUSION

The effect of macro- and microstructural features on the general and localized corrosion behavior of Alloy 625 obtained by means LPBF and MFFF were investigated. The results can be summarized as follows:

- The microstructure is strictly dependent upon the manufacturing technology adopted. In particular, the microstructure of MFFF specimen comprises equiaxial austenite grains coarser than hot rolled alloy 625.
- MFFF-built specimens were characterized by a higher porosity than LPBF with the evidence of continuous

pattern of defects due to incomplete densification of the green part during the sintering process.

- Intergranular corrosion susceptibility tests carried revealed higher corrosion rate of MFFF sample, but only superficial and no high penetrating attack was observed.
- Potentiodynamic tests in H_2SO_4 1N and neutral chloride solution showed a passive behavior of Alloy 625 over a wide range of potential, thus confirming the very high corrosion resistance in these environments.
- In acidified chloride solution at pH 3 the presence of crevice attack on MFFF specimens was detected.

REFERENCES

[1] ASTM International. ASTM G28-02(2015): Standard Test Methods for Detecting Suscepti-bility to Intergranular Corrosion in Wrought, Nickel-Rich, Chromium-Bearing Alloys. 2016; Available from: https://www.astm.org/g0028-02r15.html
[2] ASTM International. ASTM G5-14(2021): Standard Reference Test Method for Making Po-tentiodynamic Anodic Polarization Measurements. 2021; Available from: https://www.astm.org/g0005-14r21.html
[3] Sandhu SS, Shahi AS. Metallurgical, wear and fatigue performance of Inconel 625 weld claddings. J Mater Process Technol. 2016 Jul 1;233:1–8.
[4] Yin ZF, Zhao WZ, Lai WY, Zhao XH. Electrochemical behaviour of Ni-base alloys exposed under oil/gas field environments. Corros Sci. 2009 Aug;51(8):1702–6.
[5] Brownlee JK, Flesner KO, Riggs KR, Miglin BP. Selection and Qualification of Materials for HPHT Wells. Society of Petroleum Engineers - SPE High Pressure/High Temperature Sour Well Design Applied Technology Workshop 2005, HPHT 2005. 2005 May 17;
[6] Rai SK, Kumar A, Shankar V, Jayakumar T, Rao KBS, Raj B. Characterization of micro-structures in Inconel 625 using X-ray diffraction peak broadening and lattice parameter measurements. Scr Mater. 2004 Jul 1;51(1):59–63.
[7] Nagarajan B, Hu Z, Song X, Zhai W, Wei J. Development of Micro Selective Laser Melt-ing: The State of the Art and Future Perspectives. Engineering. 2019 Aug 1;5(4):702–20.
[8] Cabrini M, Lorenzi S, Testa C, Pastore T, Brevi F, Biamino S, et al. Evaluation of Corrosion Resistance of Alloy 625 Obtained by Laser Powder Bed Fusion. J Electrochem Soc. 2019 Jun 12;166(11):C3399–408.
[9] Cabrini M, Lorenzi S, Testa C, Brevi F, Biamino S, Fino P, et al. Microstructure and Selec-tive Corrosion of Alloy 625 Obtained by Means of Laser Powder Bed Fusion. Materials 2019, Vol 12, Page 1742. 2019 May 29;12(11):1742.
[10] ASTM International. ASTM B443-19: Standard Specification for Nickel-Chromium-Molybdenum-Columbium Alloy and Nickel-Chromium-Molybdenum-Silicon Alloy Plate, Sheet, and Strip. 2019; Available from: https://www.astm.org/b0443-19.html
[11] Material datasheet Inconel 625. Available from: https://static.markforged.com/downloads/Inconel-625.pdf
[12] ASTM International. ASTM B446-19: Standard Specification for Nickel-Chromium-Molybdenum-Columbium Alloy (UNS N06625), Nickel-Chromium-Molybdenum-Silicon Alloy (UNS N06219), and Nickel-Chromium-Molybdenum-Tungsten Alloy (UNS N06650) Rod and Bar. 2019; Available from: https://www.astm.org/b0446-19.html
[13] Marchese G, Colera G, Calignano F, Lorusso M, Biamino S, Minetola P, et al. Characteriza-tion and Comparison of Inconel 625 Processed by Selective Laser Melting and Laser Metal Deposition, Adv. Eng. Mater., 19: 1600635, 2016. https://doi.org/10.1002/adem.201600635
[14] Lutton Cwalina K, Demarest CR, Gerard AY, Scully JR. Revisiting the effects of molyb-denum and tungsten alloying on corrosion behavior of nickel-chromium alloys in aqueous corrosion. Curr Opin Solid State Mater Sci. 2019 Jun 1;23(3):129–41.

TORNA ALL'INDICE >